Journal of Materials Chemistry A

Accepted Manuscript

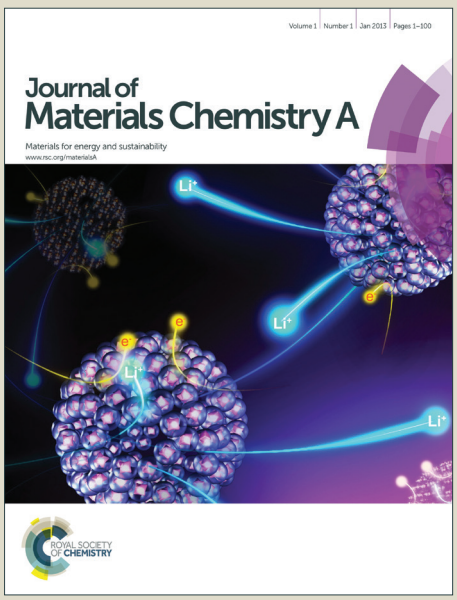

ROYAL SOCIETY OF CHEMISTRY

www.rsc.org/materialsA

Journal of Materials Chemistry A RSCPublishing

ARTICLE

Designing Thermal and Electrochemical Oxidation Processes for δ-MnO_2 Nanofibers for High-performance Electrochemical Capacitors

Cite this: DOI: 10.1039/x0xx00000x

Received 00th January 2012,
Accepted 00th January 2012

DOI: 10.1039/x0xx00000x

www.rsc.org/

Ji-Hoon Lee,[a] Tae-Youl Yang,[a] Ho-Young Kang,[a] Dae-Hyun Nam,[a] Na-Rae Kim,[a] Yoo-Yong Lee,[a] Se-Hee Lee,[b] and Young-Chang Joo*[a]

To date, the phase of electrospun MnO_x nanofibers (NFs) after thermal calcination has been limited to the low oxidation state of Mn ($x < 2$), which has resulted in insufficient specific capacitance. The organic contents in the as-spun MnO_x NFs, which are essential for forming the NF structure, make it difficult to obtain the optimum phase (MnO_2) to achieve high electrochemical performance. Herein, δ-MnO_2 NFs, which were obtained by galvanostatic oxidation of thermally calcined MnO_x NFs, were successfully fabricated while maintaining the 1-D nanoscale structure and inhibiting loss of the active materials. The galvanostatically oxidized Mn_3O_4 exhibited an outstanding performance of 380 F/g under a mass loading of 1.2 mg/cm^2. The effect of galvanostatic oxidation was strongly dependent on the concentration and energetic stability of the $Mn^{2+/3+}$ ions in the MnO_x phases.

Introduction

Electrochemical capacitors (ECs) have attracted great attention as promising devices for sustainable and environmentally-friendly energy sources. The energy density of ECs must be enhanced before they can be employed in practical applications ranging from portable electronic devices to electric vehicles (EVs). Therefore, transition metal-oxide-based electrodes, e.g., manganese,[1–5] nickel,[6] cobalt,[7] and molybdenum oxides,[8] have been intensively investigated because of the pseudocapacitance involving their valence electrons and high reversibility.[9] Manganese oxides are the most promising candidates because of their high theoretical capacitance, low cost, and natural abundance.[10, 11] The manganese in manganese oxides can assume various oxidation states; however, MnO_2 exhibits superior electrochemical performance compared with the low-valence MnO_x ($x < 2$) (Mn_3O_4 and Mn_2O_3) due to its additional capacitive mechanism, which is known as intercalation pseudocapacitance[8, 9] and constitutes the major capacitive portion of MnO_2.[12]

Previously, MnO_2 nanoparticles have been employed to increase the surface area of electrodes.[13] However, due to the agglomeration of particles, a densely packed structure was formed, resulting in a reduced specific surface area, and the electrolyte ions could not access the micropores located in the interparticular space.[14, 15] In addition, the poor interparticular contact resulted in high contact resistance. To further increase the surface area and reduce the electrical resistance, a thin layer of MnO_2 was coated on conductive carbon-based materials (activated carbon, carbon nanotubes (CNTs), and graphene).[16–18] However, because the film thickness was extremely thin, a high mass loading was not possible using this method. The effect of the electrical double layer capacitance (EDLC) of the carbon materials hardly contributed to the total capacitance because of the MnO_2 surface layers.

1-D nanofibers (NFs) are expected to achieve high capacitance and would be practical in terms of availability. The main advantage of NFs is their ability to overcome the poor cation diffusivity and electrical conductivity of Mn oxides that is the reason for their low degree of utilization.[1, 19] This advantage is a result of their high aspect ratio (length/diameter), which enhances the electrical resistance;[20, 21] their open structure, which contains well-connected

pores that allow the electrolyte to diffuse through the material; and their nanoscale dimensions, which reduce the diffusion distance. Electrospinning is currently the best-known method for fabricating 1-D nanostructures. Electrospun NFs were fabricated from a solution containing a metal (Mn) precursor and an organic matrix as a fiber former using an electrostatic repulsion force. Then, thermal calcination was performed to form the metal oxide NFs by combusting the organic content. However, the performance of manganese oxide NFs was still limited because low-valence MnO_x NFs (i.e., MnO, Mn_3O_4, Mn_2O_3, or their mixtures)[22–24] were present instead of MnO_2 after the thermal calcination. Therefore, even though the oxygen concentration was high during the calcination (a pure O_2 environment), the oxidation state of Mn of the thermally calcined manganese oxide NFs was below 4.

To increase the valence of manganese and fabricate a 1-D NF structure with the most desirable δ-MnO_2 phase, post-electrochemical oxidation of MnO_x NFs is a promising solution. To date, cyclic voltammetry (CV) oxidation methods have been widely used to oxidize low-valence MnO_x for capacitor applications.[25, 26] However, the repeated negative potential sweeps led to problems with the method: $Mn^{2+/3+}$ ions, which have finite solubility in the aqueous electrolyte,[27] were dissolved from the electrode; consequently, reoxidation and precipitation of these ions occurred at the counter electrode.[28] In this study, galvanostatic oxidation (oxidation under a constant anodic current) was employed as a post-electrochemical oxidation process. During galvanostatic oxidation, the electrode potential can be determined based on the applied current and oxidation time. Therefore, the oxidation reaction occurred at a specific potential, which could be controlled, and the oxidation of low-valence MnO_x was completed. Significantly, any dissolution process resulting in the loss of low-valence MnO_x was suppressed, enabling stable electrode construction because the continuously applied anodic current induced favored oxidizing conditions.

It should be noted that the degree to which MnO_2 was formed by galvanostatic oxidation and that the resulting electrochemical performances were largely affected by the starting phase of the thermally calcined MnO_x NFs, as determined by the electrospinning solution and thermal calcination conditions. Therefore, it is important to optimize the starting phase of MnO_x by carefully controlling these conditions. We successfully optimized the procedures to fabricate 1-D δ-MnO_2 NFs and demonstrated that these structures exhibited outstanding performance compared with that previously reported for MnO_2.[3–5]

Experimental

A. Fabrication of the electrospun MnO_x NFs

Manganese (III)-acetylacetonate (Sigma-Aldrich) was dissolved in dimethylformamide (DMF, 99.8%, Sigma-Aldrich) with the aid of acetic acid (ACS reagent, ≥ 99.7 %, Sigma-Aldrich), which promoted the solubility of the manganese precursor. Polyvinylpyrrolidone (PVP, Mw: ~ 1,300,000, Sigma-Aldrich) was also dissolved in the same mass of DMF used for dissolving manganese (III)-acetylacetonate. The two solutions were mixed together with stirring for 1 h. The compositions of the Mn precursor and organic matrix (PVP) in the combined mixture were 10 and 15 wt. %, respectively. Electrospinning was conducted with a DC voltage of 12.5 kV, feeding rate of 0.6 ml/h, and distance to the collector (Al foil) of 150 mm. The as-spun NFs were thermally calcined at 300 °C for 3 h in a furnace at a heating rate of 3 °C/min under air or ambient O_2 atmosphere.

B. Fabrication of the MnO_x NFs-based electrodes

After thermal calcination, the thermally calcined MnO_x NFs were dispersed in 30 ml of ethanol (Sigma-Aldrich) via ultrasonication, and multi-walled carbon nanotubes (MWCNTs) dispersed in ethanol (solid loading of 1 wt. %, Applied Carbon Nanotechnology Co., Korea) were added to the suspension in a mass ratio of 1/8 of that of the MnO_x NFs. The composite of MnO_x NFs + MWCNTs was obtained by evaporating the ethanol with stirring. The slurry was synthesized by adding a solution of polyvinylidene fluoride (PVDF, Mw: ~ 534,000, Aldrich) dissolved in N-methyl-2-pyrrolidone (NMP, Alfa Aesar) to the MnO_x NFs + CNT composite powder. The mass ratio of the MnO_x NFs:MWCNT:PVDF was 8:1:1. The MnO_x NF-based electrode was fabricated by coating the slurry on carbon fiber paper (CFP) (AvCarb® MGL 190, Ballard Materials Product Inc., USA) with a mass loading of 1.2 mg/cm^2 using a brush. data were collected on sputter-cleaned MnO_x NF

C. Materials characterization

The morphology of the MnO_x NFs was examined using a field-emission scanning electron microscope (SUPRA 55VP, Carl Zeiss and S4800, Hitachi) and transmission electron microscope (JEM-

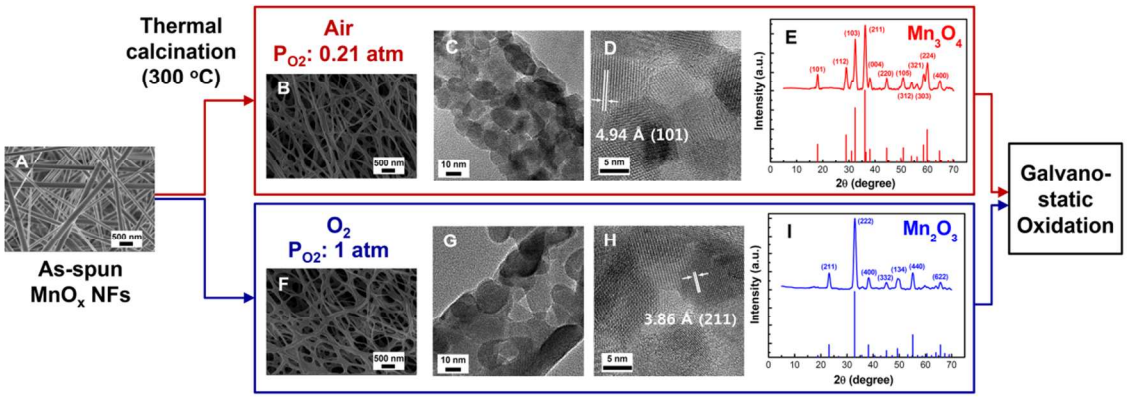

Fig. 1 The fabrication procedure of MnO_2 NFs: FE-SEM images of as-spun nanofibers (NFs) (A) and NFs calcined in air (B) and O_2 (F) and TEM and HRTEM images of NFs calcined in air (C, D) and O_2 (G, H), respectively. XRD patterns of NFs calcined in air (E) and O_2 (I) with bar-type peaks from the JCPDS cards. The plane indices corresponding to each crystallographic phase are indicated.

3000F, JEOL). The crystalline phase of the MnO_x NFs was analyzed using an X-ray diffractometer (New D8 Advance, Bruker AXS) with Cu Kα (λ = 0.154 nm) radiation. X-ray photoelectron spectroscopy data were collected on sputter-cleaned MnO_x NF surfaces using a PHI 5000 Versa Probe (ULVAC-PHI) and a monochromatic Al Kα X-ray source (1486.6 eV). The source power was maintained at 24.5 W. The mass concentration analysis on the dissolution of the Mn ions was analyzed using inductively coupled plasma-optical emission spectroscopy (ICP-OES) (720-ES, Varian).

D. Electrochemical investigation

Galvanostatic oxidation and cyclic voltammetry of the MnO_x NF-based electrode were performed in a three-electrode cell using a multichannel ZIVE MP2A (Wonatech, Korea) potentiostat/galvanostat with an aqueous 1 M Na_2SO_4 electrolyte solution (ACS reagent, ≥ 99.0 %, Sigma-Aldrich). The working electrode was the electrospun MnO_x NF-based electrode. The counter and reference electrodes were Pt foil and a saturated calomel electrode (SCE), respectively. Galvanostatic oxidation was conducted using a constant anodic current density of 0.01 mA/cm^2 for 120 h, and the oxidation process was started at the open circuit potential (OCP) of the MnO_x NFs. Cyclic voltammetry measurements were performed using a potential sweep range between 0 and 0.8 V vs. SCE for 1000 cycles, and the effect of the potential scan rate was investigated using scan rates between 5 and 100 mV/s.

Results and discussion

A. Microstructure of thermally calcined MnO_x NFs

The surface morphology of the as-spun NFs is shown in Fig. 1A. Fig. 1B - I presents micrographs and XRD patterns of the NFs thermally calcined under air (P_{O2}: 0.21 atm) and ambient O_2 (P_{O2}: 1 atm) at 300 °C. After the thermal calcination, the NF diameter decreased from ~ 200 nm (as-spun NFs, Fig. 1A) to ~ 100 nm without destroying the NF structure. In contrast to the vulnerable contacts between the as-spun NFs, strong junctions were formed between individual thermally calcined NFs. The junctions can enhance the electron transfer by reducing the contact resistance between the NFs.[29] The MnO_x NFs thermally calcined under different P_{O2} levels were both composed of equiaxial grains with an average size of ~ 12 nm. The phases of the MnO_x NFs calcined under air and ambient O_2 were Mn_3O_4 (hausmannite, JCPDS No. 01-089-0437) and Mn_2O_3 (bixbyite, JCPDS No. 01-071-0636), respectively. The HRTEM images of thermally calcined Mn_3O_4 (Fig. 1D) and Mn_2O_3 (Fig. 1F) NFs exhibit clear lattice fringes (one example of a crystallographic plane and the interplanar spacing are marked in the figure), indicating the high degree of crystallinity. The effects of the solution species, organic matrix/Mn precursor ratio, calcination temperature, and P_{O2} on the phase of the thermally calcined MnO_x NFs were also investigated (ESI† Figs. S1 - S3). When the electrospinning solution and calcination conditions were changed, only low-valence MnO_x, e.g., Mn_3O_4, Mn_2O_3, or a mixture of two phases, was obtained after thermal calcination. Therefore, the thermally calcined Mn_3O_4 and Mn_2O_3 NFs in Fig. 1 were used as representative starting materials for post-galvanostatic oxidation.

Based on the high degree of crystallinity observed from XRD (Fig. 1E and I) and thermogravimetric analysis (TGA) on as-spun NFs (ESI† Fig. S4), it was confirmed that the amount of PVP presented in thermally-calcined NFs, which were treated at 300 °C, is negligible. Therefore, post galvanostatic oxidation was not affected by the residual organic contents.

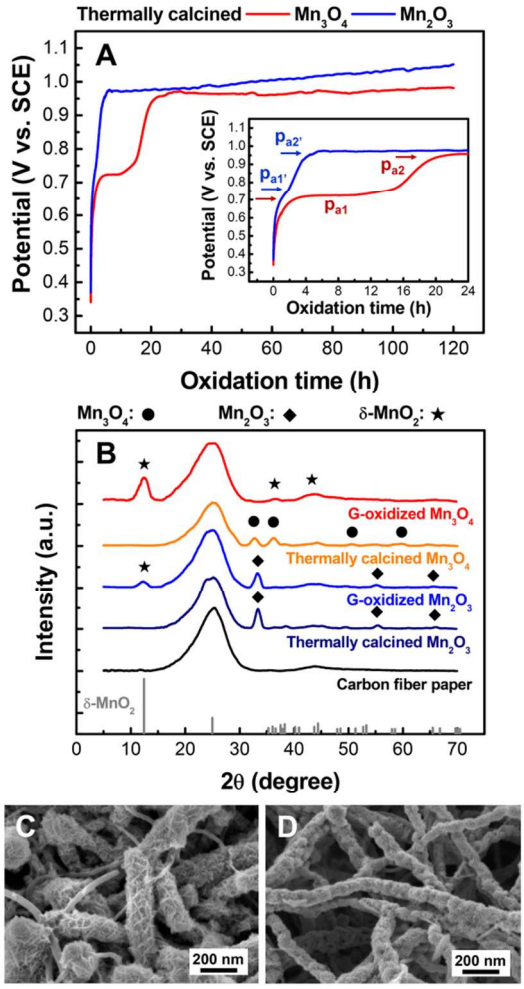

Fig. 2 (A) constant-current chronopotentiometry curves of thermally calcined Mn_3O_4 (red curve) and Mn_2O_3 (blue curve) NFs during Galvanostatic oxidation with a constant anodic current density of 0.01 mA/cm^2 (inset is chronopotentiometry curve for early stage of oxidation time). (B) XRD patterns of thermally calcined and galvanostatically-oxizdized (G-oxidized) NFs-based electrode and Carbon fiber paper. FE-SEM images of G-oxidized Mn_3O_4 (C) and Mn_2O_3 (D) NFs-based electrodes.

B. Galvanostatic oxidation of thermally calcined MnO_x NFs

Fig. 2A presents the chronopotentiometry curves during galvanostatic oxidation, which was conducted using 1 M Na_2SO_4 (pH 6.2) as the electrolyte. The amount of charges applied during the galvanostatic oxidation was the same for both NFs because the anodic current density and oxidation time were fixed to 0.01 mA/cm^2 and 120 h, respectively. In both curves, 2 regions of potential plateaus are observed: the thermally calcined Mn_3O_4 and Mn_2O_3 NFs exhibit plateau potentials of 0.73 and 0.95 V (denoted as p_{a1} and p_{a2}) and 0.74 and 0.97 V (denoted as p_{a1}' and p_{a2}'), respectively. The plateau regions in the chronopotentiometry curves indicate that faradaic electrochemical reactions occurred consistently in this region. Therefore, it can be assumed that the oxidation of both MnO_x NFs proceeded through a 2-step mechanism. The existence of a 2-step mechanism for the electrochemical oxidation of MnO_x NFs is confirmed by comparing the first 2 cycles of the cyclic voltammograms of the MnO_x NF electrode/CFP and the CFP-only samples (ESI†, Figs. S5 and S6).

The oxidation of low-valence $Mn^{2+/3+}$ ions to high-valence Mn^{4+} (MnO_2) ions was proposed to occur according to the following mechanism:[30]

$$Mn^{2+} \rightarrow Mn^{3+} + e^- \quad (1)$$

$$Mn^{3+} + 2H_2O \rightarrow MnOOH + 3H^+ \rightarrow MnO_2 + 4H^+ + 4e^- \quad (2)$$

According to the report, the electrode potential of reaction (1) is lower than that of reaction (2). The 1st (p_{a1} and p_{a1}') and 2nd (p_{a2} and p_{a2}') plateau regions correspond to reactions (1) and (2), respectively. The degree of transformation is proportional to the amount of charges used in the oxidation process, and the charge is related to the product of the current density and the duration time of the potential plateaus. Therefore, the amount of charges used in the oxidation of thermally calcined Mn_3O_4 was greater than that used to oxidize Mn_2O_3, indicating that Mn_3O_4 was more completely transformed into MnO_2.

Fig. 2B presents the XRD patterns for the thermally calcined and galvanostatically oxidized (denoted "G-oxidized") Mn_3O_4 and Mn_2O_3 electrodes. In the XRD pattern of the G-oxidized Mn_3O_4 NFs, all the peaks corresponding to the Mn_3O_4 phase disappeared, and the peaks associated with the δ-MnO_2 phase (birnessite, JCPDS No. 01-073-7864), which has a layered structure, appeared at 12.4º, 36.1º, and 48.5°. However, for the G-oxidized Mn_2O_3 NFs, Mn_2O_3 was still present, and a weak peak at 12.4° corresponding to δ-MnO_2 appeared. The phase of G-oxidized Mn_3O_4 was confirmed to be δ-

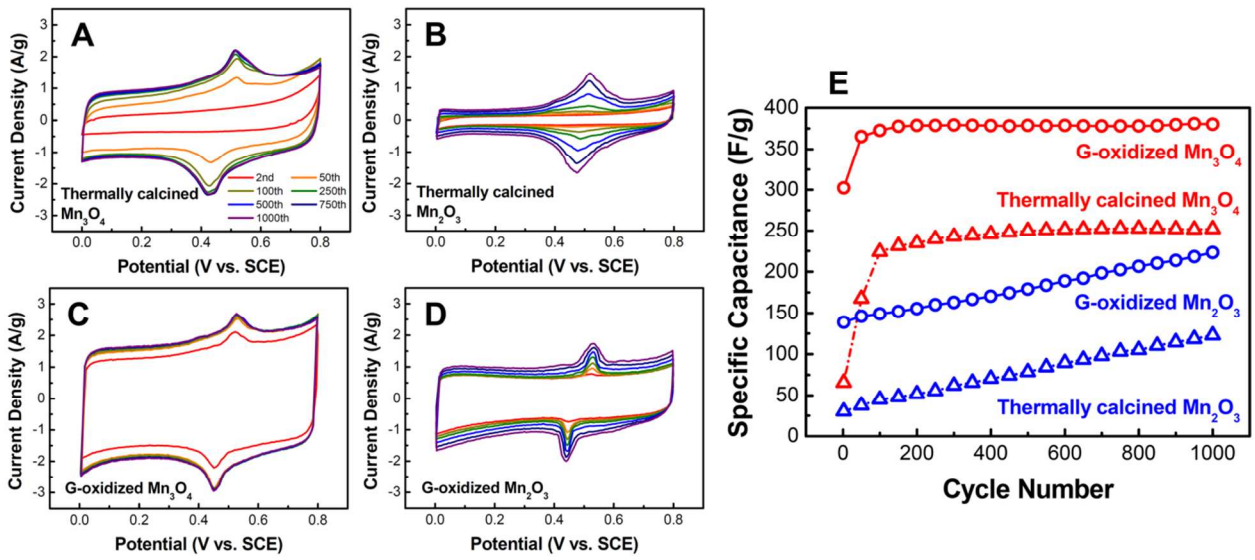

Fig. 3 Cyclic voltammograms of thermally calcined Mn_3O_4 (A) and Mn_2O_3 (B) NFs and G-oxidized Mn_3O_4 (C) and Mn_2O_3 (D) NFs with a scan rate of 5 mV/s. (E) Changes in the specific capacitance as a function of the cycle number (5 mV/s).

MnO_2, while the G-oxidized Mn_3O_4 phase was a mixture of δ-MnO_2 and Mn_2O_3.

The changes in the surface morphologies after the galvanostatic oxidation process are observed in Figs. 2C and D. Both G-oxidized MnO_x NFs formed petal-like nanosheets. Thin sheets and plates are typical features of δ-MnO_2.[31] Due to the open NF networks structures and consequent high accessibility of cations from any direction, even at high electrode mass loading, it is possible that all the MnO_x lattice sites were transformed by the galvanostatic method. The degree of the morphological changes was clearly different depending on the starting phase. The width of the G-oxidized Mn_3O_4 NFs (Fig. 2C) increased relative to that of the thermally calcined Mn_3O_4 NFs. It is expected that the G-oxidized Mn_3O_4 NFs had a significantly larger specific surface area because the increase in the width was solely caused by the formation of thin nanosheets. However, the width of the G-oxidized Mn_2O_3 NFs was almost the same as that of the thermally calcined one.

C. Electrochemical performances of G-oxidized and thermally calcined MnO_x NFs

Cyclic voltammetry (CV) measurements of the NF electrodes were performed at a scan rate of 5 mV/s for 1000 cycles, as shown in Figs. 3A - D, and the specific capacitance (Fig. 3E) as a function of cycle number was calculated from the cyclic voltammograms using the following equation:

$$\text{Specific capacitance (F/g)} = \frac{\int i/m \, dV}{2 \cdot \nu \cdot \Delta V} \qquad (3)$$

where, i, m, ν, and ΔV are the response current, mass of the total electrode, scan rate, and range of the potential scan, respectively.

The changes in the shapes of the cyclic voltammograms and the specific capacitances of the G-oxidized and thermally calcined NFs with cycling are clearly different. First, for the G-oxidized NFs (Figs. 3C and D), 1 pair of redox peaks was observed from the beginning cycle, while the pair appeared after the 50th cycle for the thermally calcined NFs (Figs. 3A and B). The pair of redox peaks (0.51 and 0.43 V for the anodic and cathodic peaks, respectively) observed in the cyclic voltammograms is related to the intercalation process that occurs in the van der Waals gaps of δ-MnO_2.[31, 32] Second, the specific capacitance of the thermally calcined MnO_x NFs, which is proportional to the integrated area of the cyclic voltammograms, gradually increased with the cycle number (Fig. 3E), e.g., the specific capacitance of the thermally calcined Mn_3O_4 NFs gradually increased up to 500 cycles, at which point it became saturated. However, for the G-oxidized Mn_3O_4 NFs, the specific capacitance was almost unchanged, and that of the G-oxidized Mn_2O_3 NFs underwent relatively smaller changes.

More importantly, the electrochemical performance of both phases was greatly improved by galvanostatic oxidation: the specific capacitances of Mn_3O_4 and Mn_2O_3 at the 1000th cycle were enhanced from 250 to 380 F/g and 123 to 223 F/g, respectively. The superior performance of the G-oxidized MnO_x NFs was also supported by investigating the color change of the electrolyte and by applying inductively coupled plasma-optical emission spectroscopy (ICP-OES) (ESI†, Fig. S7 and Table S4, respectively). After the

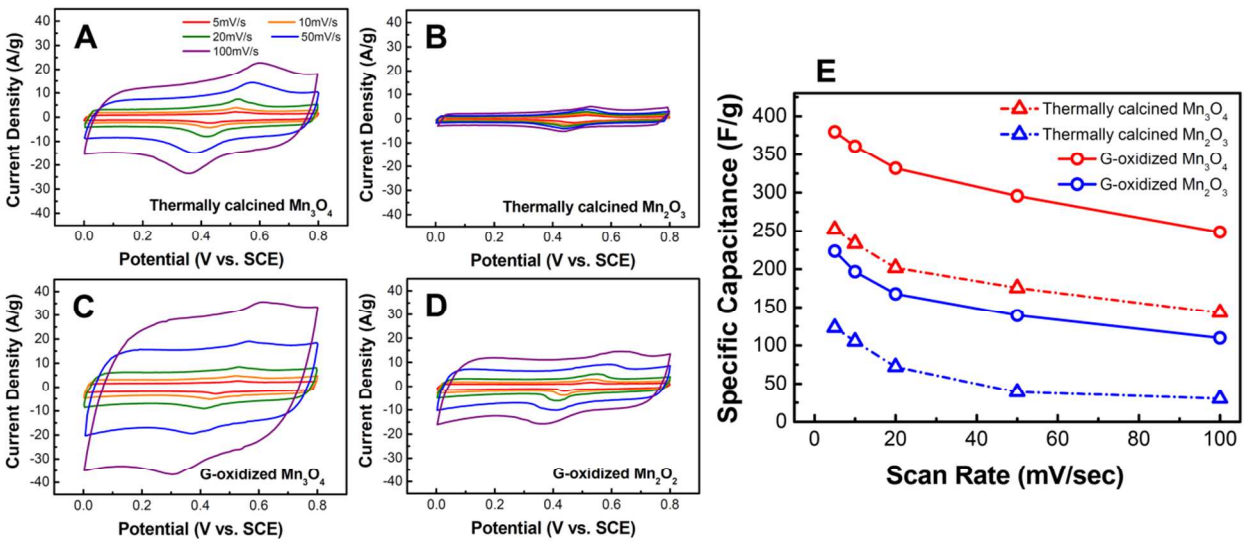

Fig. 4 Cyclic voltammograms of the 1000th cycle of thermally calcined Mn_3O_4 (A) and Mn_2O_3 (B) NFs and G-oxidized Mn_3O_4 (C) and Mn_2O_3 (D) NFs as a function of the scan rate. (E) Changes in the specific capacitance at the 1000th cycle as a function of the scan rate.

cycling of thermally-calcined Mn_3O_4, the electrolyte turned dark brown in color, and a large amount of precipitates was formed in the electrolyte. The precipitates were formed by the chemical reactions between the dissolved Mn ions and oxygen supplied by the counter electrode or dissolved in the electrolyte. The capacitance of the thermally calcined Mn_3O_4 NFs gradually increased during cycling, which is consistent with previous reports for CV-oxidized Mn_3O_4,[25, 26] indicating that the phase transformation by CV oxidation proceeded gradually. Therefore, the dissolution of $Mn^{2+/3+}$ ions from the untransformed Mn_3O_4 occurred continually until the capacitance was saturated. The color of the electrolyte after galvanostatic oxidation, however, remained transparent. The G-oxidized Mn_3O_4 NFs exhibited only slight color changes without any noticeable precipitates after cycling. The concentration of dissolved Mn ions after CV of the thermally calcined Mn_3O_4 was 4 times larger than that for the G-oxidized NFs (ESI†, Table S4).

In comparing the performances with respect to the starting phase, the specific capacitance of the Mn_3O_4 NFs was higher than that of the Mn_2O_3 NFs at every cycle investigated, and that of the Mn_2O_3 NFs did not become saturated. In addition, the redox peaks for the thermally calcined Mn_2O_3 (Fig. 3B) were broader than those for the thermally calcined Mn_3O_4, indicating that the cation migration was confined to the surface [8]. Because a periodic tunnel structure was absent for the MnO_x, this material exhibited poorer cation migration kinetics than δ-MnO_2. Based on these results, it can be concluded that the transformation rate of Mn_2O_3 into δ-MnO_2 was slower than that of Mn_3O_4, and the transformation was not complete after 1000 cycles. Therefore, the smaller amount of δ-MnO_2 in Mn_2O_3 was responsible for the lower specific capacitance.

It is noted that the G-oxidized Mn_3O_4 NF electrode is promising compared with previously reported MnO_x structures, e.g., Mn_3O_4 nanorods on graphene sheets (~ 114 F/g with 2.0 mg/cm^2),[3] hydrothermally grown MnO_2 on CNT textiles (~ 200 F/g with 0.8 mg/cm^2),[4] and MnO_2/CNT/PEDOT-PSS nanocomposites (200 F/g, with 1.5 mg/cm^2)[5] considering the mass loading of the electrode was ~ 1.2 mg/cm^2..

Figs. 4A - D present the CVs of MnO_x NFs after 1000 cycles obtained using various scan rates. Up to a scan rate of 100 mV/s, the rectangular shape of the CVs, which is a general feature of electrochemical capacitors, was well maintained for all the MnO_x NFs. Therefore, it is confirmed that facile cation migration kinetics were achieved in the NF networks due to the open structure with well-connected pores. The specific capacitance is plotted as a function of the scan rate in Fig. 4E. At every scan rate investigated, the specific capacitance of the G-oxidized MnO_x NFs was greater than that of the thermally calcined NFs. The capacitance retentions (the ratio of $C_{100\ mV/s}$ /$C_{5\ mV/s}$ (%)) for thermally calcined Mn_3O_4 and Mn_2O_3 were 56.7 and 24.5 %, and those for G-oxidized Mn_3O_4 and Mn_2O_3 were 65.4 and 49.2 %, respectively. For both starting phases, the retention was improved by galvanostatic oxidation because the number of cycles required to saturate the specific capacitance of the CV-oxidized NFs (or the thermally calcined NFs) increased as the scan rate increased. In addition, the improvement in the capacitance retention due to galvanostatic oxidation was greater for the Mn_2O_3

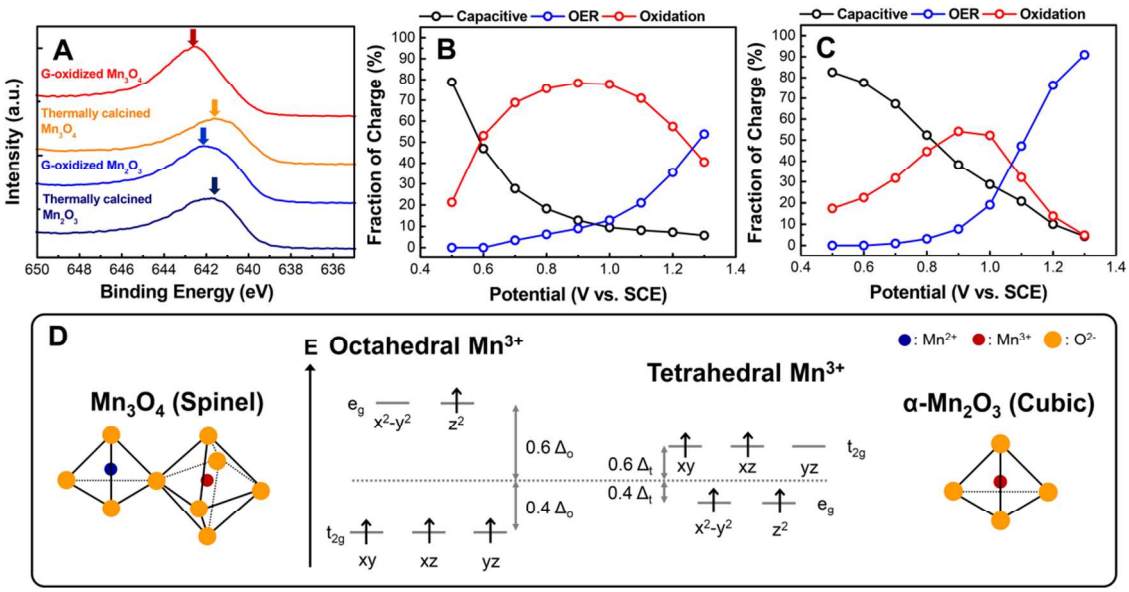

Fig. 5 (A) XPS Mn 2p 3/2 core level survey spectra for G-oxidized and thermally calcined MnO_x NFs. Changes in the fractions of capacitive, oxidation, and oxygen evolution reaction (OER) charges for thermally calcined Mn_3O_4 (B) and Mn_2O_3 (C) NFs as a function of the electrode potential. (D) Atomic structure and electronic configuration of the Mn^{3+} ions in Mn_3O_4 and Mn_2O_3.

NFs. As mentioned earlier, the transformation rate of Mn_2O_3 was kinetically slower than that of Mn_3O_4. Therefore, G-oxidized Mn_2O_3 exhibited a superior rate capability compared with thermally calcined Mn_2O_3, which was the dominant phase of Mn_2O_3.

D. The effect of starting phase of thermally calcined MnO_x NFs

The difference in the phase transformation degree of Mn_3O_4 and Mn_2O_3 during galvanostatic oxidation was closely related to the energetic stability of the Mn ions in each MnO_x. The stability in terms of the electronic configuration was determined from the sublattice structure surrounding the ions. Therefore, it is important to investigate the relationship between the changes in the chemical state of the MnO_x NFs and their crystallographic structure. The chemical state of the MnO_x NFs before and after galvanostatic oxidation was investigated using XPS, as shown in Fig. 5A and Table 1. The Mn $2p_{3/2}$ core level spectra are presented in Fig. 5A. The thermally calcined Mn_3O_4 and Mn_2O_3 exhibited peaks at a binding energy of ~ 641.8 eV, which corresponds to $Mn^{2+/3+}$.[33, 34] After galvanostatic oxidation, the binding energy peak positions were shifted to higher values. For the G-oxidized Mn_3O_4 NFs, the binding energy was ~ 642.6 eV, indicating the presence of high-valence Mn^{4+} ions.[35] The shift in the G-oxidized Mn_2O_3 peak was less remarkable than that in the G-oxidized Mn_3O_4 NFs peaks. Additionally, the average oxidation states of Mn during galvanostatic oxidation were evaluated from the splitting width of the doublet peaks in the Mn 3s core level spectra[36] (ESI†, Fig. S8) and are listed in Table 1. The average valences of Mn of the thermally calcined Mn_3O_4 and Mn_2O_3 NFs were 2.62 and 2.90, respectively, which are lower than the theoretical values (Mn_3O_4: 2.67, Mn_2O_3: 3.00). This discrepancy was caused by the oxygen vacancies in the MnO_x lattice. For G-oxidized Mn_3O_4 and Mn_2O_3, the oxidation states of Mn were 3.92 and 3.31, respectively. It was confirmed that the G-oxidized Mn_2O_3 consisted of a mixture of Mn^{4+} and untransformed Mn^{2+} or Mn^{3+} ions, while the G-oxidized Mn_3O_4 was almost fully transformed into δ-MnO_2.

The fraction of charges involved in the galvanostatic oxidation process as a function of the electrode potential is shown in Figs. 5B and C. The fraction was calculated by separating the total charges into 3 types: oxidation, capacitive, and oxygen evolution reaction (OER). Details of the calculation are described in ESI† section 7 and Fig. S9. The oxidation charge related to the phase transformation of Mn_3O_4 (77.6 %) was larger than that of Mn_2O_3 (45.4 %) based on the electrode potential at the end of the galvanostatic oxidation (Mn_3O_4: 0.97 V, and Mn_2O_3: 1.05 V).

As observed in Fig. 5D, hausmannite (Mn_3O_4) has a spinel structure containing Mn^{2+} and Mn^{3+} ions that fill tetrahedral sites with a probability of 1/8 (8 sites/unit cell) and octahedral sites with a probability of 1/2 (16 sites/unit cell), respectively. Bixbyite (Mn_2O_3)

Table 1 Average oxidation state of Mn and hydration contents of thermally calcined and G-oxidized MnO_x NFs measured from XPS data of Mn 3s core level spectra.

materials	Mn 3s core level spectra			
	upper peak (eV)	lower peak (eV)	splitting width (eV)	avg. oxidation state
thermally calcined Mn_3O_4	89.26	83.73	5.53	2.62
G-oxidized Mn_3O_4	88.88	84.01	4.87	3.92
thermally calcined Mn_2O_3	89.20	83.81	5.39	2.90
G-oxidized Mn_2O_3	89.03	83.85	5.18	3.31

has a cubic structure containing Mn^{3+} ions with O^{2-} ions in 3/4 of the tetrahedral sites. This oxide is a well-known representative nonstoichiometric oxide material with oxygen deficiencies.[37] The 1st potential plateau (Fig. 2A) or oxidation step was more prominent for Mn_3O_4 because of the difference in the Mn^{2+} ion concentration. Theoretically, 33.3 % of the Mn ions in Mn_3O_4 are Mn^{2+}, whereas the Mn^{2+} concentration in Mn_2O_3, which is determined by the oxygen vacancy concentration, is small. Two-types of Mn^{3+} ions was involved in reaction (2): ions generated by the oxidation of Mn^{2+} (reaction (1)) and those in the low-valence MnO_x. The differences in the 2nd oxidation step were caused by differences in the energetic stability of the Mn^{3+} ions in each phase, as determined by the asymmetry of the molecular orbital spin and the structure of the interstitial site. For the spinel Mn_3O_4, the Mn^{3+} ion occupies an octahedral site and has a d^4 high spin electron configuration (Fig. 5D). The partially filled degenerate set of electrons in the e_g level (axial orbitals) was involved in the degeneracy directly heading to the ligands (oxygen ion). According to the Jahn-Teller theory, this type of sublattice configuration is considered to be energetically unstable. Therefore, it was more favorable for the Mn^{3+} ions in the Mn_3O_4 phase to be transformed into a more stable, higher oxidation state, e.g., Mn^{4+}, under galvanostatic oxidation. The crystal energy splitting configuration, i.e., the positions of the e_g and t_{2g} levels of the tetrahedral system, is opposite to that of the octahedral system because the t_{2g} orbitals (d_{xy}, d_{xz}, d_{yz}) exhibit higher electron-electron repulsion. Consequently, the Mn^{3+} ions in Mn_2O_3 have unpaired electrons in the t_{2g} levels, although the ions have the same d^4 high spin electron configuration as Mn^{3+} in Mn_3O_4. In addition, none of the 5 d-orbitals of the Mn^{3+} ions at the tetrahedral site of Mn_2O_3 are directly oriented toward the oxygen ions because the Mn^{3+} ions are surrounded by only 4 oxygen ions in that system. Therefore, the energy stabilization due to the Jahn-Teller effect is not as large for the Mn^{3+} ion in Mn_2O_3 as for that in the octahedral system (Mn_3O_4). Therefore, under galvanostatic oxidation, phase transformation for the Mn_3O_4 phase was more favorable, while Mn_2O_3 underwent a relatively slow transformation.

Conclusions

In conclusion, δ-MnO_2 NFs were successfully fabricated by galvanostatically oxidizing thermally calcined MnO_x NFs. The galvanostatic oxidation greatly restricted the dissolution of Mn ions during the phase transformation, which is a major issue for CV oxidation, and the 1-D network structure was well maintained during the process. The resulting δ-MnO_2 NFs not only exhibited high surface areas due to formation of petal-like nanosheets but also exhibited facile cation migration due to the open NF network structures with well-connected pores and the $1\times\infty$ tunnel structure of δ-MnO_2. The G-oxidized Mn_3O_4 NFs (δ-MnO_2 NFs) demonstrated their capacity for excellent performance in electrochemical capacitor applications. The relative energetic instability of the Mn^{3+} ions in Mn_3O_4 compared with that in Mn_2O_3 led to a more reactive response to the galvanostatic oxidation process and a faster phase transformation. This facile fabrication method establishes an important avenue for designing and optimizing nanostructured electrode materials that require the electrode integrity during phase transformation to be maintained.

Acknowledgements

This research was supported by the Converging Research Center Program through the Ministry of Science, ICT and Future Planning, Korea (2013K000206).

Notes and references

[a] Department of Materials Science & Engineering, Seoul National University, Seoul 151-744, Korea.
[b] Department of Mechanical Engineering, The University of Colorado at Boulder, Boulder, CO 80300-0427, USA.

† Electronic Supplementary Information (ESI) available: [details of any supplementary information available should be included here]. See DOI: 10.1039/b000000x/

1 X. Lang, A. Hirata, T. Fujita and M. Chen, *Nat. Nanotechnol.*, 2011, **6**, 232-236.
2 M.-J. Deng, J.-K. Chang, C.-C. Wang, K.-W. Chen, C.-M. Lin, M.-T. Tang, J.-M. Chen and K.-T. Lu, *Energy Environ. Sci.*, 2011, **4**, 3942-3946.
3 J. W. Lee, A. S. Hall, J.-D. Kim and T. E. Mallouk, *Chem. Mater.*, 2012, **24**, 1158-1164.
4 L. Hu, W. Chen, X. Xie, N. Liu, Y. Yang, H. Wu, Y. Yao, M. Pasta, H. N. Alshareef and Y. Cui, *ACS Nano*, 2011, **5**, 8904-8913.
5 Y. Hou, Y. Cheng, T. Hobson and J. Liu, *Nano Lett.*, 2010, **10**, 2727-2733.
6 J.-H. Kim, K. Zhu, Y. Yan, C. L. Perkins and A. J. Frank, *Nano Lett.*, 2010, **10**, 4099-4104.
7 C. Yuan, L. Yang, L. Hou, L. Shen, X. Zhang and X. W. Lou, *Energy Environ. Sci.*, 2012, **5**, 7883-7887.
8 T. Brezesinski, J. Wang, S. H. Tolbert and B. Dunn, *Nat. Mater.*, 2010, **9**, 146-151.
9 B. E. Conway, *Electrochim. Acta*, 1992, **38**, 1249-1258.
10 T. Brousse, M. Toupin, R. Dugas, L. Athouël, O. Crosnier and D. Bélanger, *J. Electrochem. Soc.*, 2006, **153**, A2171-A2180.
11 A. J. Roberts and R. C. T. Slade, *Energy Environ. Sci.*, 2011, **4**, 2813-2817.
12 D. Zhai, B. Chengjun, H. Du, Y. He, C. Wei and F. Kang, *J. power sources*, 2011, **196**, 7860-7867.
13 S.-C. Pang and M. A. Anderson, *J. Mater. Res.*, 2000, **15**, 2096-2106.
14 P. Simon and Y. Gogotsi, *Nat. Mater.*, 2008, **7**, 845-854.
15 D. Qu, *J. Power Sources*, 2002, **109**, 403-411.
16 X. Dong, W. Shen, J. Gu, L. Xiong, Y. Zhu, H. Li and J. Shi, *J. Phys. Chem. B*, 2006, **110**, 6015-6019.
17 A. E. Fischer, K. Pettigrew, D. R. Rolison, R. M. Stroud and J. W. Long, *Nano Lett.*, 2007, **7**, 281-286.
18 M. N. Patel, X. Wang, B. Wilson, D. A. Ferrer, S. Dai, K. J. Stevenson and K. P. Johnston, *J. Mater. Chem.*, 2010, **20**, 390-398.
19 H. Zhang, G. Cao and Y. Yang, *Energy Environ. Sci.*, 2009, **2**, 932-943.
20 L. Hu, H. S. Kim, J.-Y. Lee, P. Peumans and Y. Cui, *ACS Nano.*, 2010, **4**, 2955-2963.
21 L. Hu, H. Wu and Y. Cui, *MRS Bull.*, 2011, **360**, 760-765.
22 C. Shao, H. Guan, Y. Liu, X. Li and X. Yang, *J. Solid State Chem.*, 2004, **177**, 2628-2631.
23 Q. Fan and M. S. Whittingham, *Electrochem. Solid-state Lett.*, 2007, **10**, A48-A51.
24 T.-S. Hyun, J.-E. Kang, H.-G. Kim, J.-M. Hong and I.-D. Kim, *Electrochem. Solid-state Lett.*, 2009, **12**, A225-A228.
25 C.-C. Hu, Y.-T. Wu and K.-H. Chang, *Chem. Mater.*, 2008, **20**, 2890-2894.
26 D. P. Dubal, D. S. Dhawale, R. R. Salunkhe and C. D. Lokhande, *J. Electroanal. Chem.*, 2010, **647**, 60-65.
27 A. Kozawa and J. F. Yeager, *J. Electrochem. Soc.*, 1965, **112**, 959-963.
28 D. Y. Qu, B. E. Conway, L. Bai, Y. H. Zhou and W. A. Adams, *J. Appl. Electrochem.*, 1993, **23**, 693-706.
29 H. Wu, L. Hu, M. W. Rowell, D. Kong, J. J. Cha, J. R. McDonough, J. Zhu, Y. Yang, M. D. McGehee and Y. Cui, *Nano Lett.*, 2010, **10**, 4242-4248.
30 A. D. Cross, A. Morel, T. F. Hollenkamp and S. W. Donne, *J. Electrochem. Soc.*, 2011, **158**, A1160-A1165.
31 S. Devaraj and N. Munichandraiah, *J. Phys. Chem. C*, 2008, **112**, 4406-4417.
32 O. Ghodbane, J.-L. Pascal, N.-L. Wu and F. Favier, *ACS Appl. Mater. Inter.*, 2009, **1**, 1130-1139.
33 B. J. Tan, K. J. Klabunde and P. M. A. Sherwood, *J. Am. Chem. Soc.*, 1991, **113**, 855-861.
34 V. D. Castro and G. Polzonetti, *J. Electron. Spectrosc. Relat. Phemon.*, 1989, **48**, 117-123.
35 B. N. Ivanov-Emin, N. A. Nevskaya, B. E. Zaitsev and T. M. Ivanova, *Zh. Neorg. Khim.*, 1982, **27**, 3101-3104.
36 M. Chigane and M. Ishikawa, *J. Electrochem. Soc.*, 2000, **147**, 2246-2251.
37 A. F. Wells, *Structural Inorganic Chemistry*, Oxford University Press, London, UK, 3rd edn., 1962.

A table of contents

Designing Thermal and Electrochemical Oxidation Processes for δ-MnO_2 Nanofibers for High-performance Electrochemical Capacitors

*Ji-Hoon Lee,[a] Tae-Youl Yang,[a] Ho-Young Kang,[a] Dae-Hyun Nam,[a] Na-Rae Kim,[a] Yoo-Yong Lee,[a] Se-Hee Lee,[b] and Young-Chang Joo[*a]*

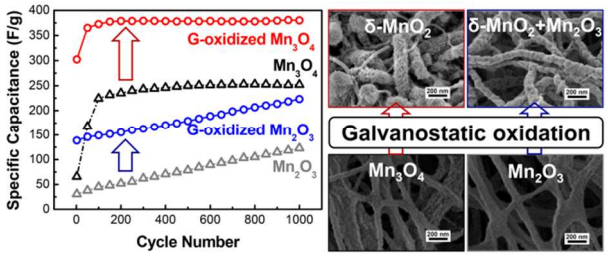

Description of TOC

δ-MnO_2 nanofibers (NFs), fabricated by galvanostatic oxidation of low valence MnO_x (X < 2) NFs, exhibited greatly improved specific capacitance.

Captions of Figures and Table

Fig. 2 The fabrication procedure of MnO_2 NFs: FE-SEM images of as-spun nanofibers (NFs) (A) and NFs calcined in air (B) and O_2 (F) and TEM and HRTEM images of NFs calcined in air (C, D) and O_2 (G, H), respectively. XRD patterns of NFs calcined in air (E) and O_2 (I) with bar-type peaks from the JCPDS cards. The plane indices corresponding to each crystallographic phase are indicated.

Fig. 2 (A) constant-current chronopotentiometry curves of thermally calcined Mn_3O_4 (red curve) and Mn_2O_3 (blue curve) NFs during Galvanostatic oxidation with a constant anodic current density of 0.01 mA/cm^2 (inset is chronopotentiometry curve for early stage of oxidation time). (B) XRD patterns of thermally calcined and galvanostatically-oxizdized (G-oxidized) NFs-based electrode and Carbon fiber paper. FE-SEM images of G-oxidized Mn_3O_4 (C) and Mn_2O_3 (D) NFs-based electrodes.

Fig. 3 Cyclic voltammograms of thermally calcined Mn_3O_4 (A) and Mn_2O_3 (B) NFs and G-oxidized Mn_3O_4 (C) and Mn_2O_3 (D) NFs with a scan rate of 5 mV/s. (E) Changes in the specific capacitance as a function of the cycle number (5 mV/s).

Fig. 4 Cyclic voltammograms of the 1000th cycle of thermally calcined Mn_3O_4 (A) and Mn_2O_3 (B) NFs and G-oxidized Mn_3O_4 (C) and Mn_2O_3 (D) NFs as a function of the scan rate. (E) Changes in the specific capacitance at the 1000th cycle as a function of the scan rate.

Fig. 5 (A) XPS Mn 2p 3/2 core level survey spectra for G-oxidized and thermally calcined MnO_x NFs. Changes in the fractions of capacitive, oxidation, and oxygen evolution reaction (OER) charges for thermally calcined Mn_3O_4 (B) and Mn_2O_3 (C) NFs as a function of the electrode potential. (D) Atomic structure and electronic configuration of the Mn^{3+} ions in Mn_3O_4 and Mn_2O_3.

Table 1 Average oxidation state of Mn and hydration contents of thermally calcined and G-oxidized MnO_x NFs measured from XPS data of Mn 3s core level spectra.